VUB VRIJE UNIVERSITEIT BRUSSEL

A search for flavour changing neutral currents involving a top quark and a Z boson, using the data collected by the CMS collaboration at a centre of mass of 13 TeV

Van Parijs, Isis

Proefschrift ingediend met het oog op het behalen van de academische graad Doctor in de Wetenschappen.

Published in Faculteit Wetenschappen & Bio-ingenieurswetenschappen
Vrije Universiteit Brussel
At 1. June 2017.

Responsible Contact: I. Van Parijs
Intitute for High Energy Physics

	First Referee:	Prof. Dr. J. D’Hondt
9	Date of Hand-in:	1 June 2017
	Date of Defense:	1 October 2017

Contents

1 Theoretical bases

1.1 Elementary particles and forces

1.2 Standard Model Lagrangian

1.3 Physics beyond the standard model

1.3.1 Effective field theory

1.3.2 Motivations for new physics

1.3.3 Searches beyond the Standard Model

1.3.4 Experimental and theoretical constraints

1.4 Statistics for a high energy particle physiscist

1.4.1 Boosted decision trees

1.4.2 Confidence levels

1.4.3 Combine limit setting tool

Experimental setup 2

The main objective of the Large Hadron Collider (LHC) was the search for the Brout-Englert-Higgs boson (or scalar boson). It was known from the Linear Electron Positron and Tevatron experiments that the scalar boson mass had to be larger than 114 GeV[1, 2], and smaller than around 1 TeV due to unitarity and perturbativity constraints [3]. On top of this, the search of supersymmetry or dark matter where part of the motivation for building the LHC. Since the start of its operation, the LHC is pushing the boundaries of the Standard Model, putting the best limits on physics beyond the Standard Model as well as precision measurements of the parameters of the Standard Model. One such an accomplishment is the discovery the scalar boson in 2012 by the two largest experiments at the LHC [4, 5].

In the first part of this chapter, the LHC and the acceleration process for protons to reach their design energies is discussed. The second part presents the Compact Muon Solenoid.

2.1 The Large Hadron Collider

The LHC has started its era of cutting edge science on 10 September 2008 [6] after approval by the European Organisation of Nuclear Research (CERN) in 1995 [7]. Installed in the previous Large Electron Positron collider (LEP) tunnels, the LHC consists of a 26.7 km ring, that is installed between 45 and 170 m under the French-Swiss border between Cessy (France) and Meyrin (Switzerland). Built to study rare physics phenomena at high energies, the LHC has the possibility to accelerate two type of particles - protons or ions Pb^{45+} - and provides collisions at four points of interaction. At the interaction points, experiments are installed in order to study the collisions.

As can be seen in Figure 2.1, the LHC is last element in a chain of creation, injection and acceleration of protons. Protons are obtained by ionising hydrogen and injected in a linear accerator (LINAC 2), where they obtain an energy of 50 MeV. They continue to the proton synchrotron booster (PSB or Booster), where the proton packets are accelerated to 1.4 GeV and are split up in twelve. The proton synchrotron (PS) increases their energy to 25 GeV before handing the protons to the super proton synchrotron (SPS), where the proton reach an energy of 450 GeV. Each accelerator ring increases in radius in order to reduce the energy loss of the protons by synchrotron radiation. This energy loss is proportional to the fourth power of the proton energy and inversely proportional to the bending radius. The protons are then injected into opposite directions into the LHC, where they are accelerated to 3.5 TeV (in 2010 and 2011), 4 TeV (in 2012 and 2013) or 6.5 TeV (in 2015 and 2016) [8]. Before the start up of the LHC in 2010, the previous energy record was held by the Tevatron collider at Fermilab, colliding proton with antiprotons at $\sqrt{s} = 1.96$ TeV.

The beam has a bunch structure obtained by the injection scheme and properties of the dump system. These bunches are obtained in the PS with 25 ns spacing. The operation of accelerating and transfering to the LHC is repeated 12 times for each counter-rotating beam. When completly filled, the LHC nominally contains 2220 bunches in run II, compared to 1380 in run I (design: 2200). At full intensity, it would have nearly 2800 bunches but this is limited due to SPS.

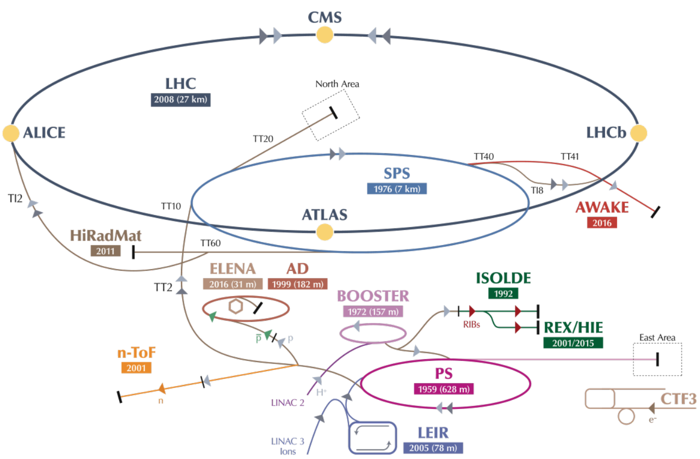

Figure 2.1: Schematic representation of the accelerator complex at CERN [9]. The LHC (dark blue) is the last element in chain of accelerators. Protons are successively accelerated by LINAC 2, the Booster, the Proton Synchrotron (PS) and the Super Proton Synchrotron (SPS) before entering the LHC.

The LHC is home to seven experiments that are placed on an interaction point:

- A Toroidal LHC ApparatuS (ATLAS [10]) and the Compact Muon Solenoid (CMS [11]) experiments are the two general purpose detectors at the LHC. They both have a hermetic, cylindrical structure and were designed to search for new physics phenomena as well as precision measurements of the Standard Model. The existence of two distinct experiments allows cross-confirmation for any discovery.

- A Large Ion Collider Experiment (ALICE [12]) and the LHC Beauty (LHCb [13]) experiments are focusing on specific phenomena. ALICE studies strongly interacting matter at extreme energy densities where quark-gluon plasma forms from heavy ions (Pb-Pb or p-Pb). LHCb searches for differences between matter and anti matter by means of the b quark, while focussing on CP symmetry violation.

- The forward LHC (LHCf [14]) and the TOTal cross section, Elastic scattering and diffraction dissociation Measurement (TOTEM [15]) experiments are two smaller experiments that focus on interactions where protons or heavy ions only meet while head on collisions take place. LHCf consists of two parts placed before and after ATLAS and studies particles created at very small angles. TOTEM is placed in the same cavern as CMS and performs precise measurements of the LHC luminosity.

- The Monopoles and Exotics Detector At the LHC (MoEDAL [16]) experiment is situated near LHCb and tries to find magnetic monopoles.

2.1.1 LHC design and operation

The most important quantity at the LHC is the luminosity[17]. This is a measurement of the number of collisions that can be produced in a detector per m^2 and per second. The LHC collisions create a number of events per second given by

$$N_{event} = L\sigma_{event}, \tag{2.1}$$

where σ_{event} is the cross section of the event of interest and L the machine luminosity. This luminosity depends only on the beam parameters and is for a Gaussian beam expressed as

$$L = \frac{1}{4\pi} N_b n_b f_{rev} \frac{N_b}{\epsilon_n} \left(1 + \left(\frac{\theta_c \sigma_z}{2\sigma^*}\right)^2\right)^{\frac{-1}{2}} \frac{\gamma_r}{\beta^*}. \tag{2.2}$$

The number of particles per bunch is expressed by N_b, while n_b is the number of bunches per beam, f_{rev} the revolution frequency, γ_r the relativistic gamma factor, ϵ_n the normalized transverse beam emittance - a quality for the confinement of the beam , β^* the beta function at the collision point - a measurement for the width of the beam, θ_c the angle between the two beams at the interaction point, σ_z the mean lengths of one packet, and σ^* the mean height of one packet. In Equation() 2.2), the blue part represents the stream of particles, the red represents the brilliance; and the green part represents the geometric reduction factor due to the crossing angle at the interaction point. Hence, in order to enhance the chances for exploration of rare events and thus enhancing the number of collisions. High beam energies as well as high beam intensities are required.

The peak design luminosity for the LHC in 2016 was 10^{34} 1/(m^2 s), which leads to about 1 billion proton interactions per second. In 2016, the LHC was around 10% above this design luminosity[18]. The luminosity is not a constant in time. It diminishes due to collisions between the beams, and the interaction of the protons and the particle gas that is trapped in the centre of the vacuum tubes due to the magnetic field. The intern diffusion of the beam degrades the emmitance and therefiore also the luminisity. For this reason, the mean lifetime of a beam inside the LHC is around 15 h. The integrated luminosity - the luminosity provided for a certain time range - recorded by CMS and ATLAS over the year 2016 is given in Figure 2.1.1. In Run II, the peak luminosity is 13-17 10^33 1/(cm^2 s) compared to 7.7 10^33 1/(cm^2 s) in Run I.

Inside the LHC ring [19], the protons are accelerated by the means of radiofrequenciy cavities, while 1232 magnets of approximately 15 m long, weighing 35 t esure the deflection of the beams. The cross section view of such a dipole is given in Figure 2.4. The two proton beams circulate in opposite direction in separate pipes inside of the magnet. Through the use of a strong electric

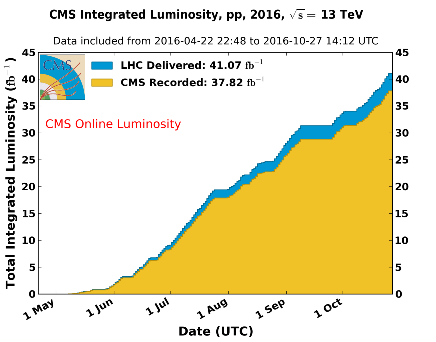

Figure 2.2: Cumulative luminosity measured online versus day delivered to (blue), and recorded by CMS (orange) during stable beams and for proton collisions at 13 TeV centre-of-mass energy in 2016. The delivered luminosity accounts for the luminosity delivered from the start of stable beams until the LHC requests CMS to turn off the sensitive detectors to allow a beam dump or beam studies. FIXME

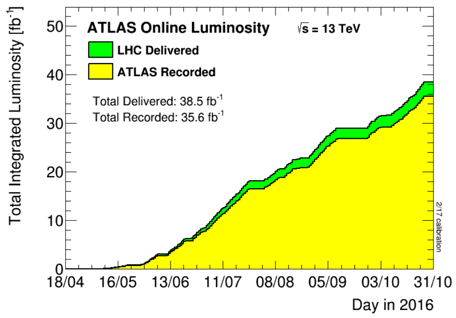

Figure 2.3: Total Integrated Luminosity in 2016 Cumulative luminosity versus time delivered to (green) and recorded by ATLAS (yellow) during stable beams for proton collisions in 2016. The delivered luminosity accounts for luminosity delivered from the start of stable beams until the LHC requests ATLAS to put the detector in a safe standby mode to allow for a beam dump or beam studies. Shown is the luminosity as determined from counting rates measured by the luminosity detectors. FIXME

current in the coils around the beam pipe, magnetic fields are generated and cause the protons to bend in the required orbits. In order to get the coil to become superconducting and able to produce - with the aid of an iron return yoke - a strong magnetic field of 8.3 T, the magnet structure is surrounded by a vessel. This vessel is filled with liquid Helium making it possible to cool down the magnet to 1.9 K. In order to get more focussed and stabilised proton beam, other higher-order multipole and corrector magnets are placed along the LHC tunnel.

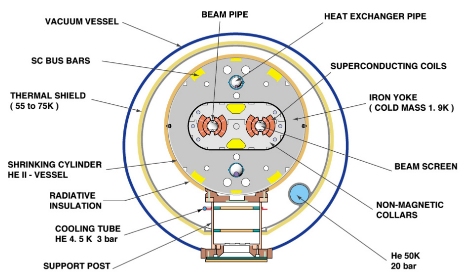

Figure 2.4: Schematic representation of the LHC dipole [20] . Two beam pipes where the proton beams circulate around the LHC ring are shown. The superconducting coils generate a magnetic field of 8.3 Tthat steer the protons in the circular path.

2.2 The Compact Muon Solenoid

At one of the collision points of the LHC, the CMS detector[21–23] is placed (see Figure 2.5). Weighing 14 000 t, This cylindrical detector is about 28.7 m long and 15 m in diameter, weighing around 14 000 t. It has an onion like structure of several specialised detectors and contains a superconducting solenoid with a magnetic field of 3.8 T. The CMS detector is designed in a way that it can address the needs of physics coming from the LHC. Living in a hadronic environment, multi-jet processes produced by the strong interaction are a main source of background for rare physics processes. Therefore, good identification, momentum resolution, and charge determination of muon, electrons and photons is one of the main goals of the CMS detector. Further it provides a good charged particle momentum resolution and reconstruction efficiency in the inner tracker such that for example jets coming from b quarks or tau particles can be identified. Also the electromagnetic resolution for an efficient photon and lepton isolation as well as a good hadronic calorimeter for the missing transverse energy were kept into account while designing CMS.

The LHC provides many collisions in a short amount of time. In order to discriminate between consecutive collisions - known as out of time pile up events - , CMS has to complete the full data acquisition for one collision event before the next one happen (around 25 ns in Run II and around 50 ns in Run I [24]). Furthermore, since the photons are in packets, around 21 in Run I and 40 in Run II inelastic collisions happen every beam crossing . This creates a great amount of background processes in the detector called in time pile up events. Due to this difficult conditions, the detector has a great granularity which on its turn creates a need for huge number of synchronized electronic channels. Furthermore, due to to high flux of particles in the regions close to the beam, the electronics has to be able to endure high radiation.

Before the start of taking collision data for 13 TeV operations on 3 June, CMS had a long shutdown (LS1)[26]. During this shut down several upgrades were performed. The innermost part of detection material in CMS (pixel) is currently made of three concentric cylindrical layers. At the end of 2016 it is upgraded by adding a fourth layer, enhancing the particle tracking capabilities of CMS. In order to be able to incorporate this new layer, the section of the beryllium beam pipe within CMS was replaced by a narrower one during LS1. For this, the pixel was removed and reinserted into CMS. In order to avoid long damage caused by the intense particle flux at the heart of CMS, the tracker is been made ready to operate at much lower temperature than before. During Run I, a small problem was detected in the electromagnetic calorimeter preshower system. For this, the preshower discs were removed, repaired and reinstalled successfully inside CMS in 2014. To help the discrimination between interesting low momentum muons coming from collisions and muons caused by backgrounds, a fourth triggering and measurement station for muons was added in each of the end caps. CMS measures the collision rate within the detector and monitors beam related backgrounds. For this, several new detectors were installed into CMS during LS1.

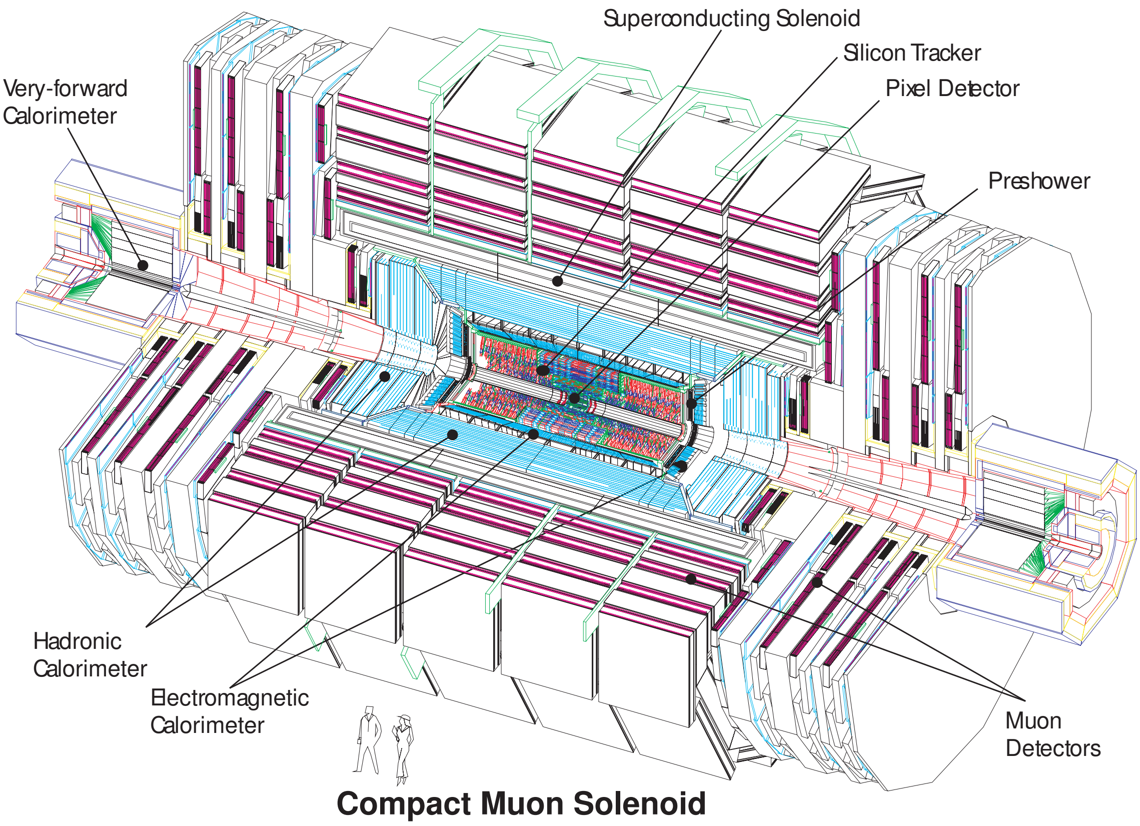

Figure 2.5: Mechanical layout of the CMS detector[25].

2.2.1 CMS coordinate system

The coordinate system used by CMS can be found in Figure 2.6. The origin of the right handed orthogonal coordinate system is chosen to be the point of collisions. The x-axis points towards the centre of the LHC ring such that the y-axis points towards the sky, and the z-axis lies tangent to the beam axis. Since the experiment has a cylindrical shape, customary coordinates are used to describe the momentum $\vec{p}$: the distance ρ, the azimuthal angle $\phi \in [-\pi, \pi]$ - the angle between the x-axis and the projection in the transverse plane of $\vec{p}$ ($\vec{p_T}$) - , the pseudo-rapidity η - expressed by the polar angle θ between the direction of $\vec{p}$ and the beam - :

$$\eta = -\ln\left(\tan\left(\frac{\theta}{2}\right)\right). \tag{2.3}$$

For the energies considered at the LHC, where $E >> m$, the pseudo-rapidity is a good approximation of the rapidity y

$$y = \frac{1}{2}\ln\left(\frac{E+p_z}{E-p_z}\right), \tag{2.4}$$

where the difference of rapidities of two particles is invariant under a Lorentz boost in the z-direction.

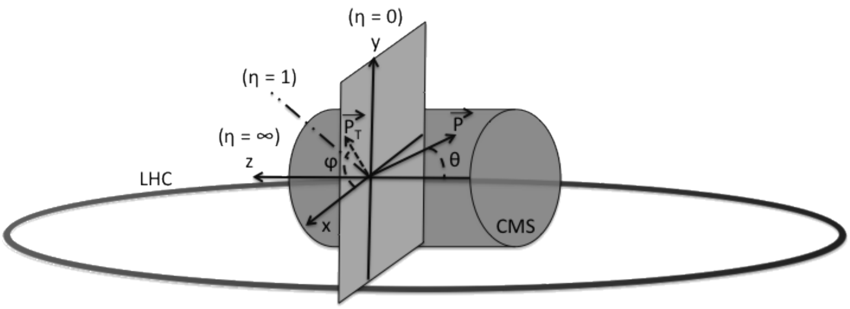

Figure 2.6: Representation of the coordinate system used by CMS. The point of origin is put at the collision point. The x-axis points towards the centre of the LHC ring such that the z-axis lies tangent to the beam axis.

2.2.2 Towards the heart of CMS

The CMS detector consists of two parts; a central barrel around the beam pipe ($|\eta| < 1.4$) and two plugs to ensure the hermeticity of the detector. In Figure 2.5 and Figure **??** the onion like structure of the CMS detector is visible. The choice of a solenoid of 12.9 m long and 5.9 m diameter gives the advantage of bending the particle trajectories in the transverse plane. The hadronic calorimeter, the electromagnetic calorimeter and the tracker are within the solenoid, while the muon chambers are placed outside the solenoid.

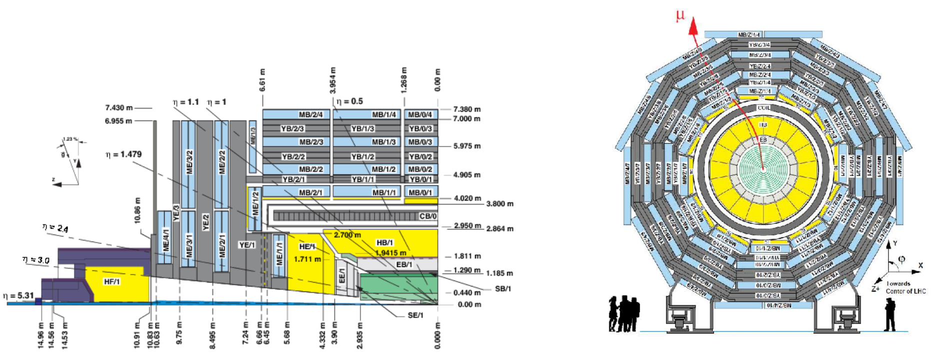

Figure 2.7: Schematic view of the CMS detector in the Run I configuration. (LEFT) Longitudinal view of one quarter of the detector. (RIGHT) Transversal view of one quarter of the detector. The muon system barrel elements are denoted as MBZ/N/S, where z= −2... + 2 is the barrel wheel number, n= 1...4 the station number and S= 1...12 the sector number. Similary, the steel return yokes are denoted as YBZ/N/S. The solenoid is denoted as CB0, while the hadronic calorimeter is denoted as HE (end cap)/ HB (barrel)/HF(forward) and the electromagnet calorimeter as EE(end cap)/EB (barrel). The green part represents the tracking system[27]

.

2.2.2.1 Muon system

The outermost part of CMS consists of the muon system. The magnet return yoke is interleaved with gaseous detector chambers for muon identifictaion nd momentum measurement. The barrel contains muon stations arranged in five separate iron wheels, while in the end cap four muon stations are mounted onto three independent iron discs in on each side. Each barrel wheel as 12 sectors in the azimuthal angle.

The muon system is divided into three parts[27], shown in Figure 2.8. The muon rate and neutron induced backgrounds are small and the magnetic field is very low for the barrel and CMS can use drift tube (DT) chambers. For the end caps however, the muon and background flux is much higher and there is a need to use cathode strip chambers (CSC) which are able to provide a faster response, higher granularity and a better resistance against radiation. In order to form a redundant trigger system, resistive plate chambers (RPC) are added. This makes a total of 250 DT chambers, 540 CSC and 610 RPC. In Figure 2.7 the arrangement is shown.

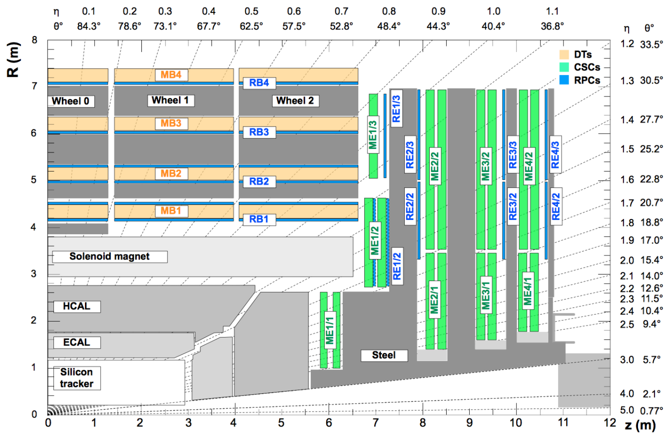

Figure 2.8: Schematic view of one quarter of the CMS muon system in the Run I configuration. [27]

.

Providing a measurement for $|\eta| < 1.2$. The DT chambers in the barrel are on average 2 × 2.5 m in size and consist of 12 layers of DT cells - 4 cm wide gas tubes with positively charged stretched wire inside - arranged in three groups of four. The $r\phi$ coordinate is provided by the two outside groups, while the middle group measures the z coordinate. For each ϕ sector, the DT chamber is mixed with the flux return yoke. For the outer muon station, the DT chamber contains only 8 layers of DT cells, providing a muon position in th $r\phi$ plane. There are four CSC stations in each end cap, providing muon measurements for $0.9 < |\eta| < 2.4$ (Run I configuration). These CSC are multi-wired proportional chambers that consist of 6 anode wire planes crossed by 7 copper strips cathode panels in a gas volume. The r coordinate is provided by the copper strips, while ϕ coordinate comes from the anode wires, giving a two dimensional position measurement. There are six layers of RPC in the barrel muon system and one layer into each of the first three stations of the end cap. They are made from two high resistive plastic plates with an applied voltage and separated by a gas volume. Read out strips mounted on top of on of the plastic plates detects the signal generated by a muon passing through the gas volume. The RPC provides a fast response with a time resolution of 1 ns and cover a range of $|\eta| < 1.8$ (Run I configuration).

During the long shutdown, the muon system underwent major upgrades [28, 29]. In the fourth station of each end cap, the outermost rings of CSC and RPC chambers were completed, providing an angular region of $1.2 < |\eta| < 1.8$ for Run II, increasing the system redundancy, and allowing tighter cuts on the trigger quality. In order te reduce the environmental noise, outer yoke discs have been placed on both sides for the end caps. At the innermost rings of the first station, the CSC has been upgraded by refurbishing the readout electronics to make use of the full detector granularity instead of groups of three (Run I).

The muon system provides triggering on muons, identifying muons and improves the momentum measurement and charge determination of high p_T muons. On top of the muon system, the muon energy is deposited in the electromagnetic calorimeter, the hadronic calorimeter, and outer calorimeter. (FIXME not tracker?) The high magnetic field enable an efficient first level trigger and allows a good momentum resolution of $\Delta^p/p \approx 1\%$ for a p_T of $100\,$ GeV and $\approx 10\%$ for a p_T of $1\,$ TeV (FIXME). There is an efficient muon measurement up to $|\eta| < 2.4$.

Muon reconstruction

The muon reconstruction[30] has three subdivision: local reconstruction, regional reconstruction and global reconstruction. The local reconstruction is performed on individual detector elements such as strip and pixel hits in the inner tracking system, and muon hits and/or segments on the muon chambers. Independent tracks are reconstructed in the inner tracker - called tracker track - and in the muon system, called standalone tracks. Based on these tracks, two reconstructions are considered. The outside-in approach is referred to as Global Muon reconstruction. For each standalone track, a tracker track is found by comparing the parameters of the two tracks propagated onto a common surface. Combining the hits from the tracker track and the standalone track, gives a fit via the Kalman filter technique [31, 32] for a global muon track. The second approach is an inside-out reconstruction, creating tracker muons. All candidate tracker tracks are extrapolated to the muon system taking into account the magnetic field, the average expected energy losses, and multiple Coulomb scattering in the detector material. When at least one muon segment - DT or CSC hits - matches the extrapolated track, the corresponding tracker track is indicated as a tracker muon.

For low transverse momenta ($p_T \lesssim 5\,$ GeV), the tracker muon reconstruction is more efficient than the global muon approach. This is due to the fact that tracker muons only require a single muon segment in muon system, while the global muon approach requires typically segments in at least two muon stations. Therefore, the global muon approach typically improves the tracker reconstruction for $p_T \gtrsim 200\,$ GeV. The tming

2.2.2.2 Solenoid

Making use of the knowledge of previous experiments of ALEPH and DELPHI at LEP and H1 at HERA, CMS choose for a large super conducting solenoid with a a length of $12.9\,$ m and a inner bore of $5.9\,$ m[23]. With 2 168 turns, a -current of $19.5\,$ kA and a total energy of 2.7 GJ, a large bending power can be obtained for a modestly-sized solenoid. In order to ensure a good momentum resolution in the forward regions, a favourable length/radius was necessary. In Figure 2.9, a photo of the CMS solenoid is given.

The solenoid uses a high-purity aluminium stabilised conductor with indirect cooling from liquid helium, together wit fully epoxy impregnation. A four-layer winding is implemented that can withstand an outward pressure of $64\,$ atm. The NbTi cable is co-extruded by pure aluminium that acts as a thermal stabilizer and has an aluminium alloy for mechanical reinforcement. The return of the magnetic field is done by fives wheels, noted by YB in Figure 2.7.

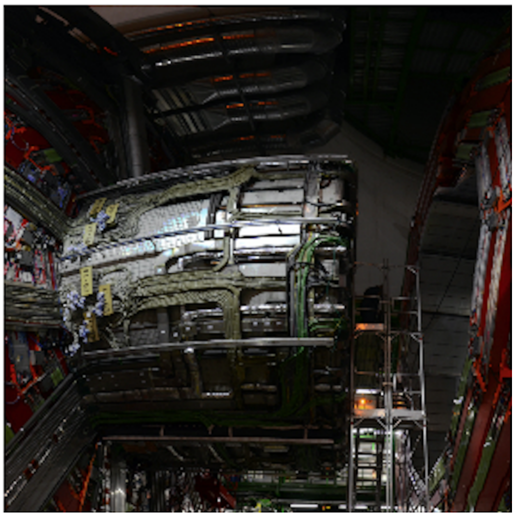

Figure 2.9: CMS solenoid during the long shutdown in 2013.

2.2.2.3 Hadronic calorimeter

The hadronic calorimeter (HCAL) is dedicated to precisely measure the energy of charged and neutral hadrons via a succession of absorbers and scintillators. This makes it crucial for physics analyses with hadronic jets or missing transverse energy. The HCAL extends between 1.77 $< r < 2.95$ m where r is the radius in the transverse plane with respect to the beam. Due to space limitations, the HCAL needs to be as small as possible and is made from materials with short interaction lengths - the length needed for absorbing 36.7% of the hadrons. The quality of the energy measurements is dependant on the fraction of the hadronic shower that can be detected. Therefore, the HCAL barrel (HB) inside the solenoid is reinforced by an outer hadronic calorimeter between the solenoid and muon detectors (HO, see Figure 2.10), using the solenoid as extra absorber. This increases the thickness to 12 interaction lengths. Furthermore, it should be as hermetic as possible and extend to large pseudo rapidity values. The HB and HO provide measurements for $|\eta| < 1.3$, while an end cap on each side (HE,$1.3 < |\eta| < 3$) and a forward calorimeter (HF, $|\eta| < 5.2$) extend the pseudo rapidity range.

The HB is made of 16 absorber plates where most of them are built from brass and others are made from stainless steal and is about five to ten intercation lengths thick. The HE is also composed of brass absorber plates and has a thickness corresponding to approximately ten interaction lengths. The HF experiences intense particle fluxes with an energy of 760 GeV deposited on average in a proton interaction at a center of mass of 14 TeV, compared to 100 GeV in the rest of the detector. Therefore, these are Cherenkov light detectors made of radiation hard quartz fibers. The main causes of such large energy events is high energy muons, cosmic particles and charged particles from late showering hadrons. During Run I, it became clear that the glass windows of the PMTs had to be replaced which was done during the long shut down [33]

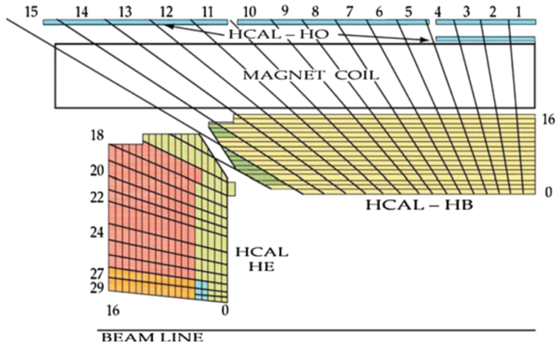

Figure 2.10: Tower segmentation for one quarter of the HCAL displayed in the rz plane[11].

2.2.2.4 Electromagnetic calorimeter

The electromagnetic calorimeter (ECAL) is designed to measure the energy of photons and electrons and covers $|\eta| < 3$. It is an hermetic, homogeneous detector and consists of 75 848 lead tungstate ($PbWO_4$) crystals. These crystals have a fast response time - 80% of the light is emitted within 25 ns - and are radiation hard. The electromagnetic showers produced by passing electrons or photons ionize the crystal atoms which emit a blue-green scintillation light, that is collected by silicon avalanche photodiodes (APDs) in the barrel and vacuum phototriodes (VPTs) in the end caps. The crystals and the APD response is sensitive to temperature changes and require a stable temperature.

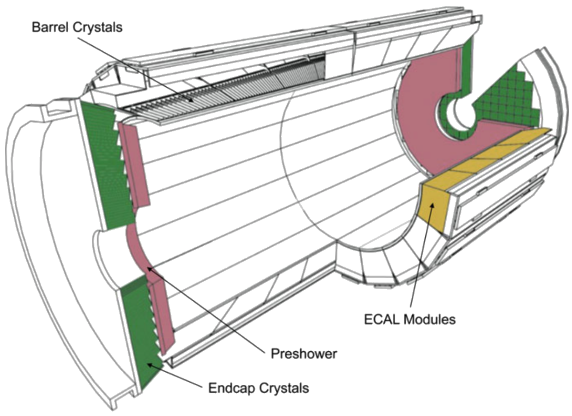

Figure 2.11: Schematic cross section of the electromagnetic calorimeter[11].

There are three regions: a central barrel (EB), a endcap region (EE) and a preshower (ES) (Figure 2.11). The EB has an inner radius of 129 cm and corresponds to a pseudo rapidity of $0 < |\eta| < 1.479$. At a distance of 314 ¢m from the vertex and covering a pseudo rapidity of $1.479 < |\eta| < 3.0$, are the EE. They consist of semi-circular aluminium plates from which structural units of 5×5 crystals (super crystals) are supported. The ES is placed in front of the crystal calorimeter over the end cap pseudo rapidity range with two planes of silicon strip detectors as active elements.

The electromagnetic shower will typically involve more then one channel. More than 90% of the energy of a 35 GeV electron or photon is contained in a 5×5 matrix of crystals. Therefore, a clustering algorithm is performed in order to associate the energy deposits to the particles impinging the calorimeter. The achieved precision[34] for the barrel is 2.10^{-3} rad in ϕ and 10^{-3} in η . For the end caps this is 5.10^{-3} rad in ϕ and 2.10^{-3} in η . The energy is reconstructed by a super cluster algorithm, taking into account energy radiated via bremsstrahlung or conversion:

$$E_{e/\gamma} = GF_{e/\gamma} \sum_{i \in cluster} S_i(t) V C_i A_i, \tag{2.5}$$

where G is the absolute energy scale in GeV/ADC, F the energy containment corrections (depends on type of particle, its energy and pseudo rapidity, eg shower leakage and bremsstrahlung losses for electrons), $S(t)$ the relative channel variation with time, C the relative channel response and A the amplitude in ADC counts. The energy resolution is given by

$$\frac{\sigma(E)}{E} = \frac{2.8\%}{\sqrt{E}} \oplus \frac{0.128}{E(GeV)} \oplus 0.3\%, \tag{2.6}$$

in the absence of a magnetic field, where the contributions come from the stochastic, noise and constant terms respectively. The dominating term is the constant term ($E_{shower} \approx 100 GeV$) and thus the performance is highly dependent on the quality of calibration and monitoring .

In Run I, the energy reconstruction happened via a weighted sum of the digitized samples[35]. For Run II however, the reconstruction had to be made more resistant for out of time pile up and a multi-fit approach has been set in to place. In this approach, the pulse shape is modelled as a sum of one in-time pulse plus the out of time pulses [34]. The energy resolution is less than 2% in the central barrel region and 2-5 % elsewhere.

2.2.2.5 Inner tracking system and operations

The tracking system (tracker) [36] is the detecting unit closest to the point of interaction. Responsible for the reconstruction of trajectories from charged particles with $|\eta| < 2.5$, being bend by the magnetic field, it provides a measurement of the momentum. The tracker is also responsible for the determination of the interaction point or vertex. It should be able to provide high granularity as well as speed, and be able to endure high radiation. For this reason, the CMS collaboration choose silicon detector technology.

The tracking system consists of a cylinder of 5.8 m long and 2.5 m in diameter. It is immersed in a co-axial magnetic field of 3.8 T due to the solenoid. As shown Figure 2.12, the tracker is built up from a large silicon strip tracker with a small silicon pixel inside. The inner region, pixel ($4.4 < r < 10.2$ cm), gets the highest flux of particles. Therefore, pixel silicon sensors of 100×150 μm is used. It consists of three cylindrical barrels that are complemented by two discs of pixel modules at each side. The silicon strip tracker ($20 < r < 116$ cm) has three subdivisions. The Tracker Inner Barrel and Discs (TIB, TID) are composed of four barrel layers accompanied by three discs at each end. The outer part of the tracker - Tracker Outer Barrel (TOB) - consists of 6 barrel layers. In the outer discs, there are nine discs of silicon sensors, referred to as Tracker End Caps (TEC).

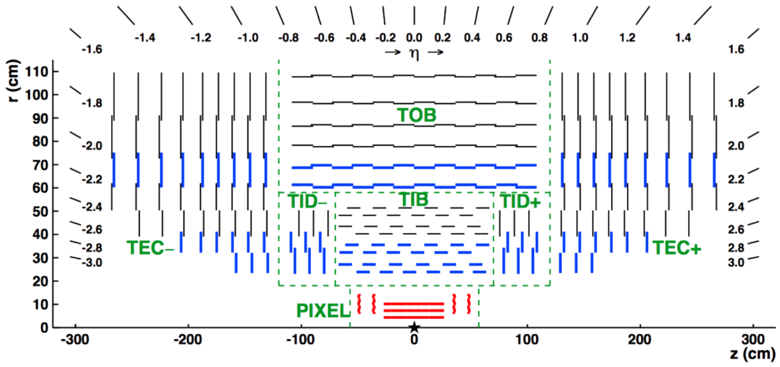

Figure 2.12: Schematic cross section of the top half of the CMS tracking system in the rz plane. The centre of tracker is shown with a star and corresponds to the approximate position of the proton collision point. The green dashed lines are an indication for each named tracker subsystem. The strip tracker modules that provide two-dimensional hits are shown by thin, black lines, while those able to reconstruct three-dimensional hit positions are shown by thick, blue lines. The pixel modules, shown in red, also provide three-dimensional hits. [22]

The pixel, shown in Figure 2.13 has 1440 modules that cover an area of about 1 m and have 66 million pixels. It provides a three-dimensional position measurement of the hits arising from the interaction from charged particles with the sensors. In transverse coordinate ($r\phi$), the hit position resolution is about 10 µm, while 20-40 µm is obtained in the longitudinal coordinate (z). The sensor plane position provides the third coordinate. The silicon strip trackers consists of 15 148 single sided modules placed in the TIB, TID and the first four rings of the TEC. They provide 9.3 million readout channels. In the TOB and the outer three rings of the TEC, double sided modules are used. These modules are constructed from two back-to-back single sided modules, where one module is rotated through a stereo angle. This covers an active area of about 198 m. The TIB and TID provide position measurements in $r\phi$ with a resolution of approximately 13-38 µm, while the TOB provides a resolution of about 18-47 µm. The resolution in the z direction is approximately 230 µm in the TIB/TID and 530 µm in the TOB. To allow overlay and avoid gaps in acceptance, each module is shifted slightly in r or z with respect to its neighbouring modules within a layer. With this detector lay out, at least nine points per charged particle trajectory can be measured in an $|\eta|$ range up to 2.4.

During the first data taking period of the LHC (2010 to 2013), the tracker operated at +4°C. With the higher LHC beam intensities from 2015 onwards, the tracker needs to be operated at much lower temperatures. This is due to the fact with intense irradiation, the doping concentration changes, the leakage current increases proportional to the fluence and the charge collection efficiency decreases due to charge trapping. Mostly the leakage current (I) is affected by the temperature change:

$$I \propto T^2 e^{-\frac{E_g}{2kT}}, \tag{2.7}$$

where T is the operating temperature, E_g the band gap and k the Boltzmann constant. There is approximately a factor 15 between the leakage currents at room temperatures and at −10 °C.

Figure 2.13: The pixel barrel being re-installed after the Long Shutdown in 2015, around the beam pipe at CMS[37]

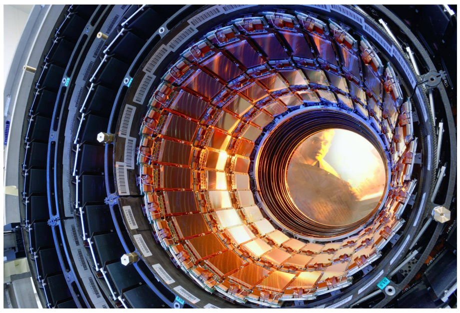

Figure 2.14: First half of the inner tracker barrel, consisting of three layers of silicon modules.[38]

During the first long shutdown (LS1), the CMS cooling plant was refurbished[39] and the fluorocarbon cooling system overhauled. To help to suppress the humidity inside the tracker, new methods for vapour sealing and insulation were applied. Furthermore, several hundred high-precision sensors are used to monitor the humidity and temperature. In order to get as dry air as possible, a new dry-gas plant provides eight times more dry gas (air or nitrogen) than during the first run, and allows regulation if the flow. As final addition, the cooling bundles outside the tracker are equipped with heater wires and temperature sensors in order to maintain safe operations above the cavern dew point For the data taking in 2015-2016, the tracker operated at $-15°$C.

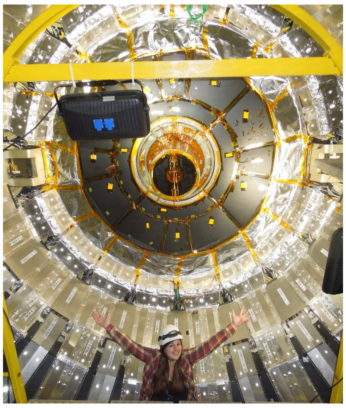

Figure 2.15: Tracker bulkhead being put into closed state with insulation pieces installed during an early trial in fall 2013

Figure 2.16: New Tracker high-capacity dry-gas plant with membrane separation system[26]

Track reconstruction

An iterative tracking algorithm is responsible for the reconstruction of the tracks made by charged particles in the inner tracking system. Each iteration consists of four steps[23]: the track-seed generation, the pattern recognition algorithm, removal of track-hit ambiguities and a final track fit.

The seed generation is the first step. It consists of finding reconstructed hits that are usable for seeding the subsequent track-finding algorithm. They are identified from a group of at least three reconstructed hits in the tracker, or from a pair of hits while requiring the origin of the track segment to be compatible with the nominal beam-collision point. Since the pixel has a higher granularity compared to the strip tracker, its seed generation efficiency is higher. The overall efficiency exceeds 99%. The second step of each iteration, the pattern recognition algorithm, uses the seeds as a starting point for a Kalman filter method [31, 32]. This algorithm extrapolates the seed trajectory towards the next tracker layer taking into account the magnetic field and multiple scattering effects. The track parameters are updated when a compatible hit in the next layer is found. This procedure continues until the outermost layer us reached. Since the Kalman filter method can result in multiple tracks associated to the same seed, or different tracks sharing the same hits, a removal of ambiguities is necessary. This ambiguity resolving is done by removing tracks that are sharing too many hits from the list of track candidates. The tracks with highest number of hits or with the lowest χ^2 if the track fit is kept. The updated track parameters are then refitted using the Kalman filter method, where all hits found in the pattern recognition step are taken into account. The fit is done twice - once outwards from the beam line towards the calorimeters, and inwards from the outermost track hit to the beam line -, improving the estimation of the track parameters.

All hits that are unambiguously associated to the final track are removed from the list of available hits. In order to associate the remaining hits, the procedure is repeated with looser track reconstruction criteria. The use of the iterative track reconstruction procedure has a high track finding efficiency, where the fake track reconstruction rate is negligible. For muons, this results in a global track reconstruction efficiency exceeding 98%, and 75-98% for charged hadrons. Due to the lack of coverage of the two pixel discs in high $|\eta|$ range, the efficiency drops.

Primary vertex reconstruction

The primary vertex reconstruction should be able to meausre the location of all proton interaction vertices in each event: the signal vertex an all vertices from pile up events. It consists of a vertex finding and a vertex fitting algorithm and happens in three steps. Tracks are selected to be consistent with being produced promptly in the primary interaction by imposing requirements on track parameters[36] By grouping reconstructed tracks according to the z coordinate of their closest approach to the beam line, vertices for all interaction in the same beam crossing are found, at CMS this is done by a deterministic annealing algorithm [40] . On top of this, a vertex fitting algorithm like the Adaptive Vertex fitter [41], is performed. This creates the three-dimensional primary-vertex position. With this fit, the contribution from long-lived hadron decays is reduced by down weighting the tracks with a larger distance to the vertex. The primary vertex corresponding to the highest sum of squared track transverse momenta is noted as the point of the main interaction. The resolution on the primary vertex is about 14 µm in $r\phi$ and about 19 µm) in the z direction for primary vertices with the sum of the track $p_T > 100$ GeV for 2016 data taking.

2.2.3 Data acquisition

At a design luminosity of $10^{34}\ 1/(\mathrm{m}^2\,\mathrm{s})$, the proton interaction rate exceeds 1 GHz. This makes it impossible for the CMS experiment to store all the data generated. For this, a two level trigger system has been put in place. The first level (Level-1) is a custom hardware system, while a second level (HLT) is software based running on a large farm of computers. In run II, with the increase in centre of mass energy and a higher luminosity a larger number of simultaneous inelastic collisions per crossing is expected with respect to run I. For this, the CMS Level-1 has been upgraded [42].

CMS Level-1 trigger

The Level-1 trigger has to be a flexible, maintainable system, capable of adapting to the evolving physics programme of CMS [43]. Its output rate is restricted to 100 kHz imposed by the CMS readout electronics. It is implemented by custom hardware and selects events containing candidate objects - eg ionization deposits consistent with a muon, or energy clusters corresponding to an electron / photon / tau lepton / missing transverse energy / jet. Collisions with large momenta can be selected by using scalar sum of the transverse momenta of the jets.

By buffering the raw data from the CMS subdetectors in front-end drivers, the level-1 trigger has a pipeline memory of 3.2 µs to decide whether to keep an event or reject it. The trigger primitives (TP) from the calorimeters and muon detectors are processed in several steps and combined into a global trigger. This information is then combined with the input from the other subsystems. The seperate inouts are synchronized to each other and the LHC orbit clock and sent to th eglobal trigger module. Here, level-1 trigger algorithms are performed within 1 µs to decide whether to keep the event.

For run II, all hardware, software, databases and the timing control system have been replaced. The main changes are that the muon system now uses the redundancy of three muon detector system earlier to make a high resolution muon trigger. The calorimeter system isn't bound any more for streaming data the data and the global trigger has more level-1 trigger algorithms.

CMS HLT trigger

The HLT is an array of commercially available computers with programmable menu that has output rate of on average 400 Hz for off-line event storage. The data processing is based on a HLT path. This is a set of algorithmic steps to reconstruct objects and make selections on them. Here, the information of all sub detectors can be used to perform algorithms on higher level reconstructed objects. (FIXME: tracker in hlt or already in L1?)

2.2.4 CMS computing model

The selected data is stored, processed and dispersed via the Worldwide Large Hadron Collider GRID (WLCG)[44, 45]. This has a tiered structure that function as a single, coherent system:.

At CERN, a single Tier-0 is located. The raw data collected by CMS is archived here, and a first reconstruction of the data is done. This data is then in a file format usable for physics analysis. Furthermore, it is able to reprocess data when new calibrations are made available. The Tier-0 site distributes this data to a total of seven Tier-1 centres. They carry out data reprocessing and store real data as well as simulated data. The Tier-1 further distribute the data to over 50 Tier-2 centres. These make the data accessible for physics analysis and are also being used for the production of simulated data. This data is accessible for physicists around the world.

3 Event generation, simulation and reconstruction

3.1 Collision event generation

3.1.1 Parton distribution functions and the hard interaction

3.1.2 Parton showering

3.1.3 Hadronization and decay

3.1.4 Underlying event

3.1.5 Event reconstruction and identification

3.2 Detector simulation

3.3 Physics object reconstruction and identification

3.3.1 The particle flow event reconstruction method

3.3.2 Identification of particles

3.3.2.1 Muon reco and ID

3.3.2.2 Electron reco and ID

3.3.2.3 Jet reco and ID of b quarks

3.3.2.4 Missing transverse energy reconstruction

3.3.3 Calibrations and corrections

4 The search for FCNC involving a top quark and a Z boson

4.1 Model assumptions

4.2 Data and simulation

4.2.1 Standard Model Background simulation

4.2.2 FCNC signal simulation

4.2.3 Trigger requirements

4.3 Baseline event selection

4.4 Data driven background estimation

4.5 Regions and channels

4.6 Construction of template distributions

4.7 Systematic uncertainties

4.8 Limit setting procedure

4.9 Result and discussion

5 Conclusion and outlook

Bibliography

[1] R. Barate et al.: **Search for the standard model Higgs boson at LEP**. In: *Phys. Lett.*, **B565**: (2003), pp. 61–75. doi: 10.1016/S0370-2693(03)00614-2. arXiv: hep-ex/0306033 [hep-ex] (see p. 3).

[2] Kenneth Herner: **Higgs Boson Studies at the Tevatron**. In: *Nucl. Part. Phys. Proc.*, **273-275**: (2016), pp. 852–856. doi: 10.1016/j.nuclphysbps.2015.09.131 (see p. 3).

[3] Abdelhak Djouadi: **The Anatomy of electro-weak symmetry breaking. I: The Higgs boson in the standard model**. In: *Phys. Rept.*, **457**: (2008), pp. 1–216. doi: 10.1016/j.physrep.2007.10.004. arXiv: hep-ph/0503172 [hep-ph] (see p. 3).

[4] Serguei Chatrchyan et al.: **Observation of a new boson at a mass of 125 GeV with the CMS experiment at the LHC**. In: *Phys. Lett.*, **B716**: (2012), pp. 30–61. doi: 10.1016/j.physletb.2012.08.021. arXiv: 1207.7235 [hep-ex] (see p. 3).

[5] Georges Aad et al.: **Observation of a new particle in the search for the Standard Model Higgs boson with the ATLAS detector at the LHC**. In: *Phys. Lett.*, **B716**: (2012), pp. 1–29. doi: 10.1016/j.physletb.2012.08.020. arXiv: 1207.7214 [hep-ex] (see p. 3).

[6] Lyndon Evans and Philip Bryant: **LHC Machine**. In: *Journal of Instrumentation*, **3**:08 (2008), S08001. url: http://stacks.iop.org/1748-0221/3/i=08/a=S08001 (see p. 3).

[7] Thomas Sven Pettersson and P Lefèvre: **The Large Hadron Collider: conceptual design**. Tech. rep. CERN-AC-95-05-LHC. Oct. 1995, p. 20 and 22. url: https://cds.cern.ch/record/291782 (see p. 3).

[8] Jorg Wenninger and Ezio Todesco: **Large Hadron Collider momentum calibration and accuracy**. Tech. rep. CERN-ACC-2017-0007. Geneva: *CERN*, Feb. 2017. url: https://cds.cern.ch/record/2254678 (see p. 4).

[9] Cinzia De Melis: **The CERN accelerator complex. Complexe des accélérateurs du CERN**. In: (July 2016). General Photo. url: https://cds.cern.ch/record/2197559 (see p. 4).

[10] G. Aad et al.: **The ATLAS Experiment at the CERN Large Hadron Collider**. In: *JINST*, **3**: (2008), S08003. doi: 10.1088/1748-0221/3/08/S08003 (see p. 4).

[11] S. Chatrchyan et al.: **The CMS Experiment at the CERN LHC**. In: *JINST*, **3**: (2008), S08004. doi: 10.1088/1748-0221/3/08/S08004 (see pp. 4, 13).

[12] K. Aamodt et al.: **The ALICE experiment at the CERN LHC**. In: *JINST*, **3**: (2008), S08002. doi: 10.1088/1748-0221/3/08/S08002 (see p. 4).

[13] A. Augusto Alves Jr. et al.: **The LHCb Detector at the LHC**. In: *JINST*, **3**: (2008), S08005. doi: 10.1088/1748-0221/3/08/S08005 (see p. 4).

[14] M. Bongi et al.: **Astroparticle physics at LHC: The LHCf experiment ready for data taking**. In: *Nucl. Instrum. Meth.*, **A612**: (2010), pp. 451–454. doi: 10.1016/j.nima.2009.08.039 (see p. 4).

[15] G. Anelli et al.: **The TOTEM experiment at the CERN Large Hadron Collider**. In: *JINST*, **3**: (2008), S08007. doi: 10.1088/1748-0221/3/08/S08007 (see p. 4).

[16] B. Acharya et al.: **The Physics Programme Of The MoEDAL Experiment At The LHC**. In: *Int. J. Mod. Phys.*, **A29**: (2014), p. 1430050. doi: 10.1142/S0217751X14300506. arXiv: 1405.7662 [hep-ph] (see p. 5).

[17] by James Gillies: **Luminosity? Why don't we just say collision rate?** In: (Mar. 2011). url: http://cds.cern.ch/record/1997001 (see p. 5).

[18] by Harriet Jarlett and Harriet Kim Jarlett: **LHC pushes limits of performance**. In: (Aug. 2016). url: http://cds.cern.ch/record/2212301 (see p. 5).

[19] Oliver Sim Brüning, Paul Collier, P Lebrun, et al.: **LHC Design Report**. CERN Yellow Reports: Monographs. Geneva: CERN, 2004. url: https://cds.cern.ch/record/782076 (see p. 5).

[20] Jean-Luc Caron: **Cross section of LHC dipole.. Dipole LHC: coupe transversale.** AC Collection. Legacy of AC. Pictures from 1992 to 2002. May 1998. url: https://cds.cern.ch/record/841539 (see p. 6).

[21] **Technical proposal**. LHC Tech. Proposal. Cover title : CMS, the Compact Muon Solenoid : technical proposal. Geneva: CERN, 1994. url: https://cds.cern.ch/record/290969 (see p. 7).

[22] G. L. Bayatian et al.: **CMS physics: Technical design report**. In: (2006) (see pp. 7, 15).

[23] G L Bayatian, S Chatrchyan, G Hmayakyan, et al.: **CMS Physics: Technical Design Report Volume 1: Detector Performance and Software**. Technical Design Report CMS. There is an error on cover due to a technical problem for some items. Geneva: CERN, 2006. url: https://cds.cern.ch/record/922757 (see pp. 7, 11, 16).

[24] by Cian O'Luanaigh: **LHC progresses towards higher intensities**. In: (Aug. 2015). url: http://cds.cern.ch/record/2051986 (see p. 7).

[25] CMS Collaboration: **Detector Drawings**. CMS Collection. Mar. 2012. url: https://cds.cern.ch/record/1433717 (see p. 8).

[26] by Corinne Pralavorio and Corinne Pralavorio: **Major work to ready the LHC experiments for Run 2**. In: (May 2015). url: http://cds.cern.ch/record/2024977 (see pp. 7, 16).

[27] S Chatrchyan, V Khachatryan, A M Sirunyan, et al.: **Performance of the CMS Drift Tube Chambers with Cosmic Rays**. In: *J. Instrum.*, **5**:arXiv:0911.4855. CMS-CFT-09-012 (Nov. 2009), T03015 . 47 p. url: http://cds.cern.ch/record/1223944 (see pp. 9–10).

[28] Luigi Guiducci: **CMS muon system towards LHC Run 2 and beyond**. Tech. rep. CMS-CR-2014-333. Geneva: *CERN*, Oct. 2014. URL: https://cds.cern.ch/record/1966038 (see p. 10).

[29] Carlo Battilana: **The CMS muon system status and upgrades for LHC run-2 and performance of muon reconstruction with 13 TeV data**. Tech. rep. CMS-CR-2016-437. Geneva: *CERN*, Dec. 2016. URL: http://cds.cern.ch/record/2239185 (see p. 10).

[30] Serguei Chatrchyan et al.: **Performance of CMS muon reconstruction in pp collision events at $\sqrt{s} = 7$ TeV**. In: *JINST*, **7**: (2012), P10002. DOI: 10.1088/1748-0221/7/10/P10002. arXiv: 1206.4071 [physics.ins-det] (see p. 11).

[31] R. Frühwirth: **Application of Kalman filtering to track and vertex fitting**. In: *Nuclear Instruments and Methods in Physics Research Section A: Accelerators, Spectrometers, Detectors and Associated Equipment*, **262**:2 (1987), pp. 444–450. DOI: http://dx.doi.org/10.1016/0168-9002(87)90887-4 (see pp. 11, 17).

[32] Pierre Billoir: **Progressive track recognition with a Kalman like fitting procedure**. In: *Comput. Phys. Commun.*, **57**: (1989), pp. 390–394. DOI: 10.1016/0010-4655(89)90249-X (see pp. 11, 17).

[33] Emrah Tiras, Burak Bilki, and Yasar Onel: **Commissioning of CMS Forward Hadron Calorimeters with Upgraded Multi-anode PMTs and μTCA Readout**. In: (2016). arXiv: 1611.05232 [physics.ins-det] (see p. 12).

[34] L. Brianza: **Precision crystal calorimetry in LHC Run II with the CMS ECAL**. In: *Journal of Instrumentation*, **12**:01 (2017), p. C01069. URL: http://stacks.iop.org/1748-0221/12/i=01/a=C01069 (see p. 14).

[35] Serguei Chatrchyan et al.: **Energy Calibration and Resolution of the CMS Electromagnetic Calorimeter in pp Collisions at $\sqrt{s} = 7$ TeV**. In: *JINST*, **8**: (2013). [JINST8,9009(2013)], P09009. DOI: 10.1088/1748-0221/8/09/P09009. arXiv: 1306.2016 [hep-ex] (see p. 14).

[36] Serguei Chatrchyan, Vardan Khachatryan, Albert M Sirunyan, et al.: **Description and performance of track and primary-vertex reconstruction with the CMS tracker**. In: *J. Instrum.*, **9**:arXiv:1405.6569. CERN-PH-EP-2014-070. CMS-TRK-11-001 (May 2014). Comments: Replaced with published version. Added journal reference and DOI, P10009. 80 p. URL: http://cds.cern.ch/record/1704291 (see pp. 14, 17).

[37] by Christine Sutton: **Chronicles of CMS: the saga of LS1**. In: (May 2015). URL: http://cds.cern.ch/record/2024986 (see p. 16).

[38] **A beautiful barrel for CMS**. In: (Mar. 2014). URL: http://cds.cern.ch/record/1998635 (see p. 16).

[39] **Cool running for CMS tracker**. In: (Mar. 2014). URL: http://cds.cern.ch/record/1998606 (see p. 16).

[40] K. Rose: **Deterministic annealing for clustering, compression, classification, regression, and related optimization problems**. In: *Proceedings of the IEEE*, **86**:11 (Nov. 1998), pp. 2210–2239. DOI: 10.1109/5.726788 (see p. 17).

[41] Wolfgang Waltenberger: **Adaptive Vertex Reconstruction**. Tech. rep. CMS-NOTE-2008-033. Geneva: *CERN*, July 2008. URL: https://cds.cern.ch/record/1166320 (see p. 17).

[42] L. Cadamuro: **The CMS Level-1 trigger system for LHC Run II**. In: *Journal of Instrumentation*, **12**:03 (2017), p. C03021. URL: http://stacks.iop.org/1748-0221/12/i=03/a=C03021 (see p. 18).

[43] Vardan Khachatryan et al.: **The CMS trigger system**. In: *JINST*, **12**:01 (2017), P01020. DOI: 10.1088/1748-0221/12/01/P01020. arXiv: 1609.02366 [physics.ins-det].

[44] Claudio Grandi, David Stickland, Lucas Taylor, Achille Petrilli, and Alain Hervé: **CMS Computing Model: The "CMS Computing Model RTAG"**. Tech. rep. CMS-NOTE-2004-031. CERN-LHCC-2004-035. LHCC-G-083. Geneva: *CERN*, Dec. 2004. URL: http://cds.cern.ch/record/814248.

[45] Christoph Eck, J Knobloch, Leslie Robertson, et al.: **LHC computing Grid: Technical Design Report. Version 1.06 (20 Jun 2005)**. Technical Design Report LCG. Geneva: CERN, 2005. URL: https://cds.cern.ch/record/840543.